 doi:10.20944/preprints202201.0389.v1

Communication

Preparation of NbAs Single Crystal by the Seed Growth Process

Yinchang Sun [1,‡], Bojin Zhao [1,‡], Zongju Huo [1], Hongjun Liu [1], Yongkuan Xu [1], Zhanggui Hu [1] and Hailong Qiu [1,*]

[1] Tianjin Key Laboratory of Functional Crystal Materials, Institute of Functional Crystal, Tianjin University of Technology, Tianjin 300384, China.
* Correspondence: qiu@tjut.edu.cn
‡ The authors contribute equally to this work

Abstract: A Weyl semimetal is a novel crystal with low-energy electronic excitations that behave as Weyl fermions. It has received worldwide interest and was believed to have opened the next era of condensed matter physics after graphene and three-dimensional topological insulators. However, it is not easy to obtain a single large-size crystal because there are many nucleations in the preparation process. Here, a bottom-seed CVT growth method is proposed in this paper, and we acquired the large-size, high-quality NbAs single crystals up to 5×4×4 mm^3 finally. X-ray diffraction and STEM confirmed that they are tetragonal NbAs, which the key is to use seed crystal in vertical growth furnace. Notably, the photoelectric properties of the crystal are obtained under the existing conditions, which paves the way for the follow-up work.

Keywords: Weyl semimetal; NbAs single crystal; Seed growth; photoelectric

1. Introduction

Weyl semimetals (WSM) have a topologically non-mediocre energy band structure and play an essential role in the study of fundamental physical properties that is a three-dimensional analog of graphene, in which the conduction and valence bands cross near the Fermi energy[1-3]. The band-crossing point, the so-called Weyl point, acts as a magnetic monopole (a singular point of Berry curvature) in momentum space and always comes in pairs[4,5]. This peculiar phenomenon makes these materials exhibit many unique properties, such as Fermi arc[3], ultra-high mobility[6], negative magnetoresistance caused by chiral anomalies[7], and broadband light response in the mid-infrared range[8].

NbAs is one of the first-class Weyl semimetal (TaAs, TaP, NbAs, NbP), which crystallizes in a body-centered tetragonal unit cell with lattice constants a = 3.452 Å, c = 11.679 Å, and the space group is $I4_1md(C_{4v}^{11})$[9,10] (as shown in Figure 1(a)). For NbAs, the melting point of Nb reaches 2468 °C, while the As (melting point: 817 °C) has the characteristics of direct sublimation without liquefaction when heated to 613 °C under pressure. Therefore, the high pressure environment is very favorable for the reaction conditions of As[11]. At the same time, NbAs, as a compound containing As, for safety reasons, the open growth system can not meet the requirements for the growth environment. Besides NbAs, other phases such as $NbAs_2$, Nb_3As, Nb_4As_3 exist in the Nb-As binary system. Therefore, in the report, the chemical vapor transport (CVT) method is usually used to grow large-size, high-quality NbAs single crystals[12].

Preprints (www.preprints.org) | NOT PEER-REVIEWED | Posted: 25 January 2022 doi:10.20944/preprints202201.0389.v1

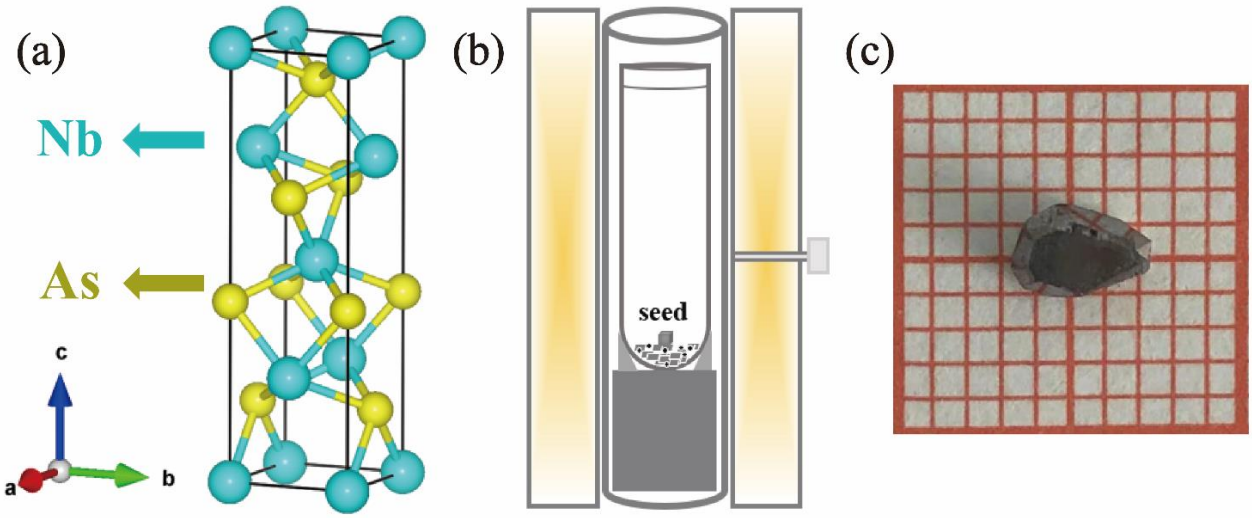

Figure 1. (a) Crystal structure of NbAs. (b) Schemes of the chemical vapor transport experiments for crystallization of NbAs in a two-step method. (c) Photograph of NbAs single crystal.

Sadly, there are always many nucleations in this process during the growth of NbAs. We believe there are two reasons. On the one hand, the transmission capacity of the raw material atmosphere is limited. On the other hand, the quartz tube's axial and radial temperature gradients are large[13,14]. As a result, the environment of raw material atmosphere during crystal growth is uneven and unstable, and the continuity of crystal growth cannot be maintained. Finally, small polycrystalline grains are obtained, which is very unfavorable to the growth of large-size crystals. This paper provides a bottom-seed crystal growth process, which solves the above problems. Firstly, the vertical CVT process growth method is used, the raw materials were placed at the bottom of the quartz tube[15]. In this case, the raw material concentration at the bottom of the quartz tube will be much greater than that at the top, which is conducive to the growth of crystals at the bottom of the quartz tube when the transport distance of gas is significantly shortened. Secondly, the volume of the growth zone used for vertical growth will be much smaller than of the horizontal CVT method, thus reducing the axial and radial temperature gradients in the growth zone and further ensuring the stability and continuity of crystal growth. In addition, the crystal with the exposed surface of (001) is added as the seed crystal, which provides a growth site for the raw material atmosphere and reduces the barrier of crystal growth. So we can think these methods are the key to obtaining large-size and high-quality crystals[16,17].

2. Materials and Methods

2.1 Synthesis of NbAs crystal

As we all know, exploring an appropriate growth process is the key to obtaining large crystals. In this work, we reported a bottom-seed CVT growth method, and Figure 1(b) shows the experimental configurations. In a typical run, Nb foil (99.99%), As (99.99%), and I_2 (99.99%) with the molar ratio of 1:1.05:0.05 were selected as raw materials, loaded in a 45 ml quartz tube, which was 14 cm in length and 2 cm in inner diameter. Meanwhile, we selected the grain of NbAs with classy crystal orientation (here, the {001} facets was selected as the growth section) as the seed, then it is added into the quartz tube together with the raw materials.

Preprints (www.preprints.org) | NOT PEER-REVIEWED | Posted: 25 January 2022 doi:10.20944/preprints202201.0389.v1

The quartz tube was initially filled with argon and sealed quickly to avoid the loss of iodine and arsenic when evacuated to a pressure below 4×10^{-4} Pa. Nb powder, Nb foil has a larger specific surface area and few defects, which is conducive to acquiring large crystals[10]. In addition, Saini et al. [18] found that As must be excessive if we want to obtain the best crystal growth effect that even for the growth of metal-rich crystals in the study of the Pd-As system. Therefore, here we add a slight excess of As to achieve the growth of NbAs single crystal. As for I_2, it plays a catalytic and transport role that is accord to the kinetic analysis of I_2 in the growth of TaAs crystal by Li[11] et al. And to avoid the explosion of quartz tube caused by the vapor pressure generated when I_2 and As sublimated to gaseous, the amount of I_2 selected is 1 mg/ml here.

Afterward, the quartz tube was heated gradually from room temperature to 1000 ℃ over 72 h, keep it for 30 days in a high-temperature environment of 1050 ℃ and finally naturally cooled down to room temperature (Although the reaction time is longer, after comparing the growth results many times, a long-term heat preservation process is essential). Through the above work, we obtained NbAs single crystals with good crystallinity, with the size of up to $4\times3\times3$ mm^3 in three-dimension (as the Figure 1(c) shown). However, we have not seen giant NbAs single-crystal reported at present.

2.2. Device Fabrication

NbAs devices are produced by dry transfer technology under argon filling conditions. With the help of an optical microscope, the tape was utilized to fix the surface of the NbAs crystal. After determining the position of the sample, use thermal evaporation to deposit Cr/Au (10 nm/70 nm) as a contact electrode. Semiconductor parameter analyzer (Keithley, 4200-SCS) and standard probe station are earmarks for electronic and photoelectric measurement. The optical response of the device was measured using a laser with adjustable power and incident wavelength.

3. Results and Discussion

3.1. Structure Analysis

Niobium arsenide, NbAs, crystallizes in a body-centered tetragonal Bravai lattice, space group $I4_1md$, point group C_{4v}. Our X-ray diffraction (XRD) obtains lattice constants of a = 3.45 Å and c = 11.68 Å, consist with earlier crystallographic studies. As shown in Figure 2(a), the upper black line in the diagram is the XRD of NbAs-powder (obtained by grinding NbAs-crystals), which is completely consistent with the data in PDF No. 17-0896 (blue line in the figure). In addition, we checked the main peak positions and marked the corresponding crystal planes. Among them, few noncorresponding crystal planes belong to polyarsenides (such as $NbAs_2$)[19,20], and their existence is temporarily unavoidable in the growth of this kind of crystal. The result shows that the grown NbAs have high purity and few miscellaneous items.

Note that the seed of NbAs, its exposed surface is mainly {001} facets, and the one-dimension length is about 1.5mm. These faces have relatively larger lattice-plane-space and, therefore, a slower growth rate and thus are found more frequently than others in the as-grown crystals[11]. Nevertheless, when we use these seed crystals for further growth, they can provide a basis for the growth of other plans in the NbAs crystal so that other poorly developed planes can be displayed.

Preprints (www.preprints.org) | NOT PEER-REVIEWED | Posted: 25 January 2022 doi:10.20944/preprints202201.0389.v1

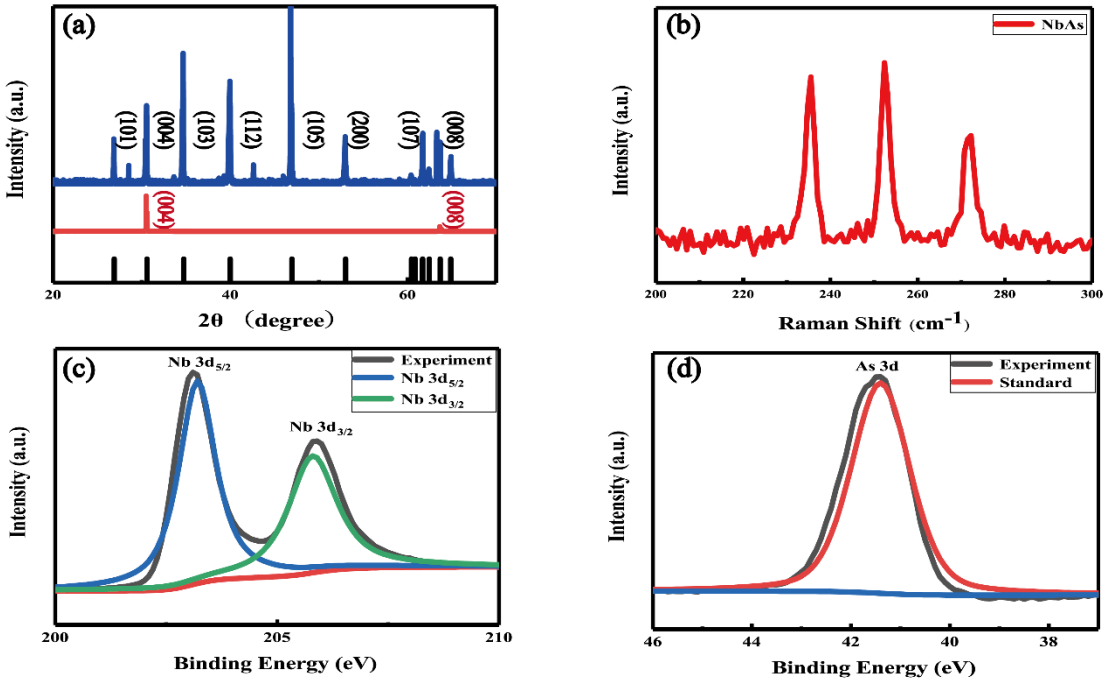

Figure 2. (a) X-ray diffraction pattern of NbAs power, and the {001} facets of NbAs single crystal. (blue line in the figure is PDF of the NbAs) (b) Raman spectra of NbAs single crystal. (c) (d) Typical XPS spectrum of Nb 3d and As 3d core level.

3.2. Material Characterization

As a widely used and powerful characterization method, Raman spectroscopy can preliminarily understand the phono information of synthetic crystals[21]. We characterized the NbAs crystals by Raman spectroscopy, shown in Figure 2(b) of bulk NbAs crystals, which mainly displayed three prominent Raman peaks in the range of 180-330 cm^{-1}. According to the previous Raman spectra of NbAs[22,23], we marked the vibration modes corresponding to the three peak positions in Figure 2(b), which are $B_1(1)$ mode at 234 cm^{-1}, $B_1(2)$ mode at 252cm^{-1}, and A_1 mode at 272cm^{-1} respectively. The spectral characterization results are consistent with the theoretical data[24,3], indicating the excellent crystalline quality of NbAs crystals.

A typical XPS (X-ray photoelectron spectroscopy) spectrum of NbAs is shown in Figures 2(c) and (d). The experimental data were labeled by consulting the literature and comparing the database, i.e., Nb $3d_{5/2}$ at 203.1 eV and Nb $3d_{3/2}$ at 205.8 eV. The pair has an energy splitting of ~2.7 eV[22], which is consistent with our expectation for the spin-orbit-split $3d_{5/2}$ and $3d_{3/2}$ levels of Nb core levels. Similarly, the XPS data of As at the low binding energy end is consistent with the reported, indicating that the 41.5 eV belongs to the 3d orbit of As.

As a means of characterizing crystal quality and structure, atomic morphology characterization can more intuitively and accurately reflect the specific information of Nb and As atoms in NbAs crystals. Figure 3(a) is a typical STEM image that shows clear lattice stripes, and Figure 3(b) is a low-power SEM image of bulk NbAs placed on an ultra-thin carbon film. The test results say that the spacing between (001) and (010) is about 3.4 Å, which is consistent with the data in the literature. At the same time, the diffraction points of (110) and (001) are also in the Fast Fourier Transform (FFT) diagram in Figure 3(a). Similarly, the structure of these facets was drawn in Figures 3(d) and 3(e). In the recent research of NbAs crystals, the coexistence of hexagonal and tetragonal phases was discussed. The observation or characterization of NbAs single crystal on the atomic scale shows that the crystal is not a single phase structure[9].

Preprints (www.preprints.org) | NOT PEER-REVIEWED | Posted: 25 January 2022 doi:10.20944/preprints202201.0389.v1

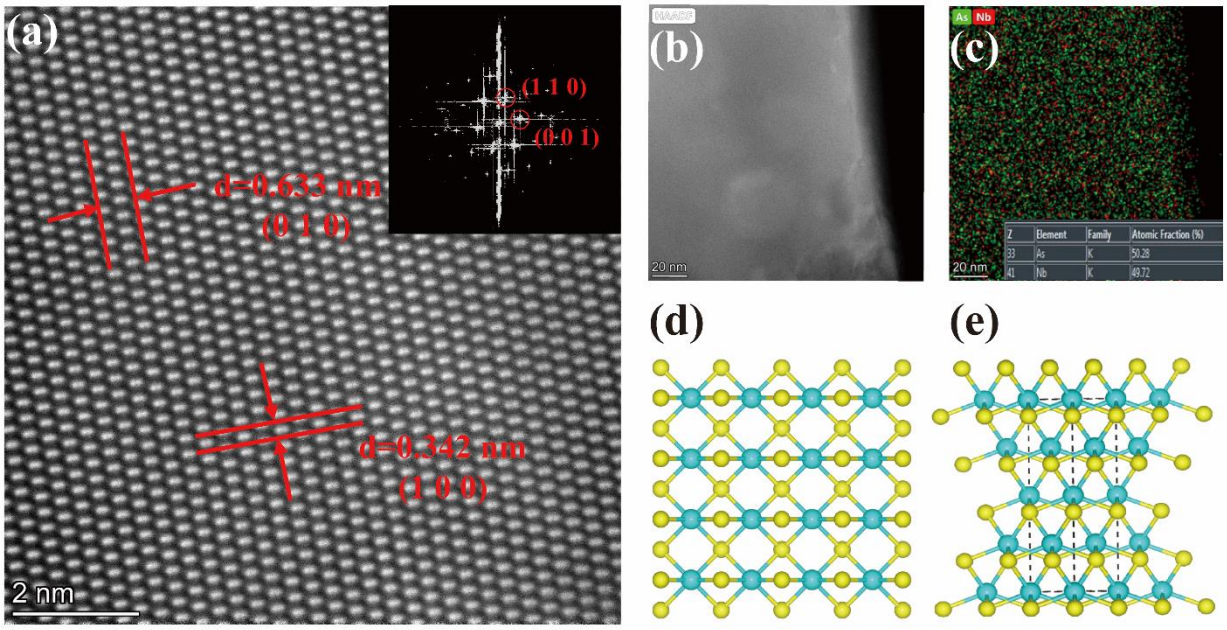

Figure 3. (a) HAASF-STEM images of NbAs single crystal. (the illustration is FFT pattern) (b) TEM images of bulk NbAs placed on an ultra-thin carbon film. (c) EDS mapping of bulk NbAs. (d) and (e) show the (001) and (110) facets of NbAs single crystal.

In our experiments, the coexistence phase problem was overcome by improving the bottom-seed method and synthesizing the high-quality NbAs crystals with a single-phase structure, highlighting our work's significance. The EDS (energy dispersion spectrum) is shown in Figure 3(c), in which the uniform distribution of Nb and As atoms can be seen. The illustration also indicated that Nb: As is close to 1:1. This information proved the high quality of our crystals on the micro-scale.

3.3. Photoelectric response detection of NbAs crystal

As for the photoelectric response of NbAs, the photodetection of TaAs can be used as a reference[25]. Inspired by TaAs broadband photodetection and the inherent limitations of the experimental environment, we only investigated a photo-detecting prototype made by Weyl semimetal NbAs in a visible light region (550 nm-800 nm) at room temperature.

After evaporation, the tape is carefully torn off, and the area covered by the tape becomes the device channel of the unevaporated electrode. The optical microscope photo of the device is shown in Figure 4(a). The dark current (I) is measured under an applied voltage (V) that varies from -0.1 to 0.1 V. The I-V curve is shown in Figure 4(b). The linearity of the curve indicates that the Schottky barrier at the contact interface between the TaAs sample and the Cu electrode is shallow. Therefore, the incident light is usually projected on the (001) surface, as shown in the red circle marked area in Figure 4(a). NbAs absorb photons, then causes electron transitions and generate carriers, leading to the generation of photocurrent, the difference between current under light and dark. In order to form a good comparison with TaAs, we also measured the time-resolved light response of the NbAs device at a source-drain voltage of 0.1mV. We only list the test results under 550 nm and 800 nm lasers, as shown in Figure 4(c-d). It can be seen that the photoresponse current of NbAs is equivalent to that of TaAs (under laser conditions, the response current is in the μA level), and the switching ratio is close to 5, but the bright and dark current is relatively poor under stable conditions. We believe that, compared to the photoelectric detection of TaAs, we have not adopted data optimization processing to demonstrate the intrinsic properties of NbAs better. In addition, because our laser has poor stability at 10mW (if the laser intensity is too small, the photoresponse current of the order of μA will

Preprints (www.preprints.org) | NOT PEER-REVIEWED | Posted: 25 January 2022 doi:10.20944/preprints202201.0389.v1

be more difficult to distinguish), can not reach the TaAs photoelectric detection conditions (stable 20mW laser intensity output), so the photoresponse current is unstable. Although we cannot reach the test conditions of TaAs, the photoresponse current of the same magnitude under the same source and drain voltage conditions indicates the research potential of NbAs in wide-band photoresponse detection[25].

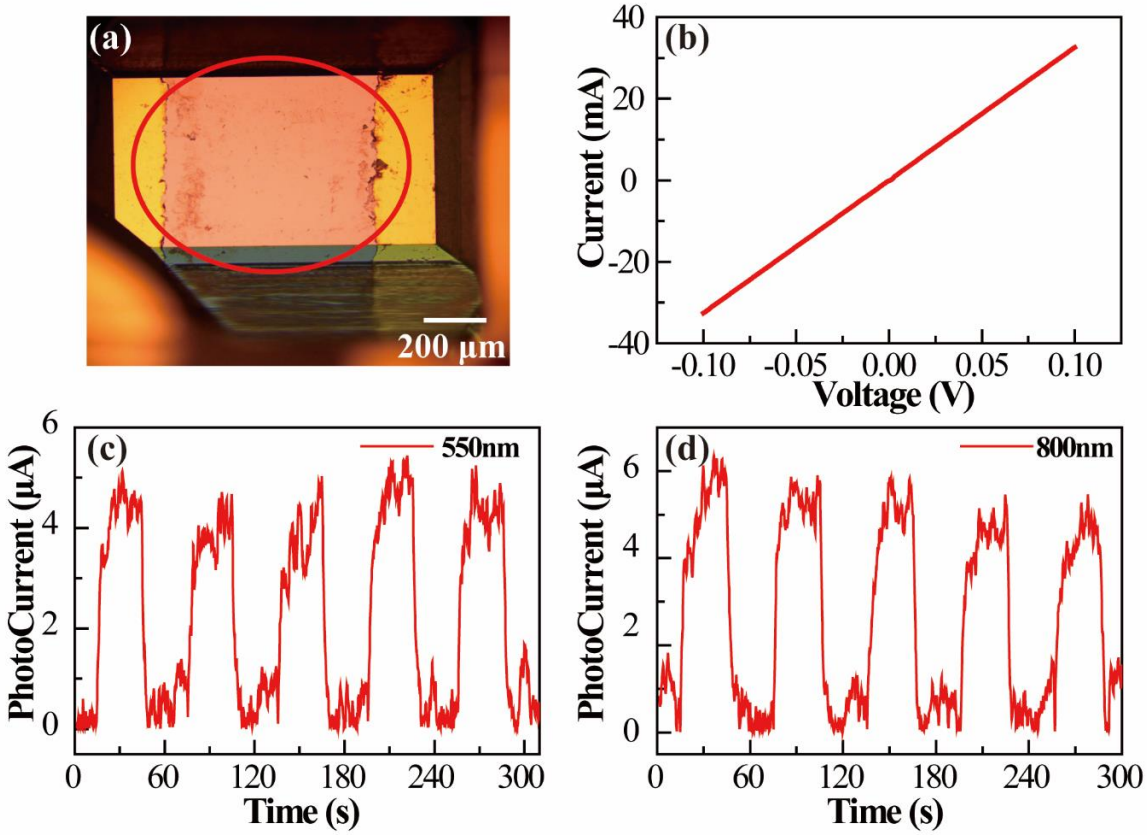

Figure 4 (a) Optical topography picture of NbAs device. (b) the I–V curve of the photodetecting prototype. (c-d) When the source-drain voltage is 0.1mV, and the incident light intensity is 10 mW, the I-T curve of the device at 550nm and 800nm incident light.

The photoelectric responsivity (R) and detection rate (D*) can be defined as[26-29]

$$R = \frac{I_{ph}}{PA} \tag{1}$$

Among them, I_{ph}, P, and A represent the photocurrent, incident optical power density, and the effective irradiation area of the detector.

$$D^* = R\sqrt{\frac{S}{2qI_{dark}}} \tag{2}$$

Where, R, S, q, and I_{dark} respectively represent the responsivity, the effective irradiation area of the heterojunction, the primary charge, and the dark current. Figure 5(a-b) lists the device's R and D* related information in the range of 550-800 nm (corresponding to the incident photon energy of 1.5 to 2.25 eV) when the incident power is fixed at 10 mW. It can be seen that R and D* do not change significantly with the incident photon energy. Except for the high responsivity at 550 nm, the responsivity is stable at 2 mA/W (D* close to 10^7 Jones). This result is close to the reported value of TaAs in the visible light band (R = 0.4~0.7 mA/W, D* = 4~7×10^8 Jones)[25]. When the incident laser wavelength is 550 nm, R and D* reached 16mA/W and 1.1×10^8 Jones, respectively. This result provides clues to its light response mechanism. It shows that NbAs have stronger absorption and more energy

Preprints (www.preprints.org) | NOT PEER-REVIEWED | Posted: 25 January 2022 doi:10.20944/preprints202201.0389.v1

scattering events at short wavelengths, which helps to achieve a more significant light response. In addition, more incredible energy is transferred from the absorbed photons to the electrons excited on the short-wavelength side.

It is worth noting that, according to reports[25], TaAs have a broad-spectrum light response from visible range to the long-infrared range at room temperature. As for NbAs, we only conducted preliminary tests on its light response in the visible light range, and its broadband light response at room temperature still needs more in-depth theoretical and experimental research.

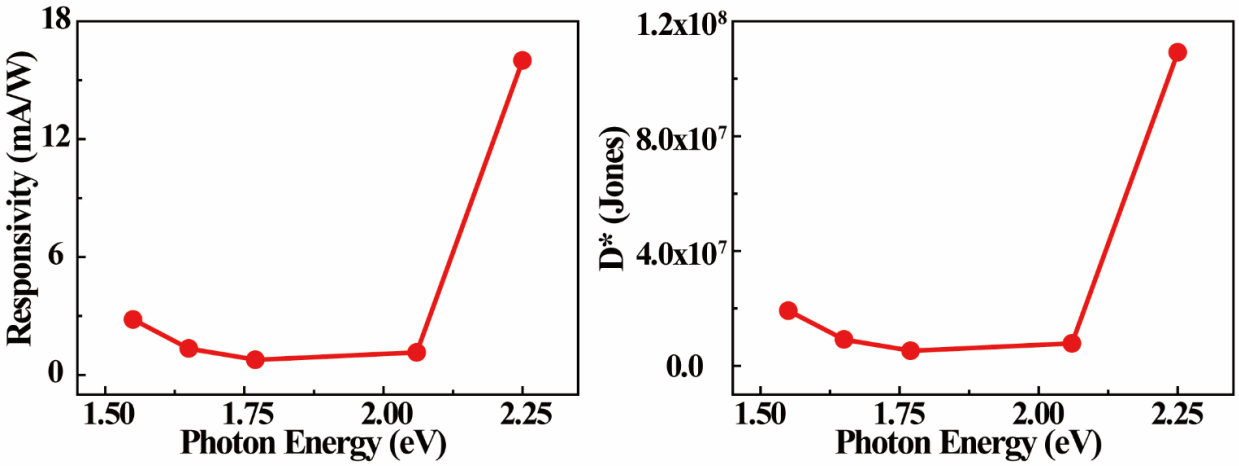

Figure 5 (a) Responsivity variation characteristics of NbAs photoelectric device prototype within 1.5 to 2.25 eV. (b) The relationship between the detection rate D* of NbAs devices and the energy of incident photons.

4. Conclusions

In summary, the one-dimensional size of the NbAs single crystal grown by the CVT method using the bottom seed method can reach 4 mm, and the three-dimensional size can reach 4×3×3 mm^3. The quality of the product has been confirmed by powder XRD and Raman methods. More importantly, the atomic-level morphology characterization results show that we have overcome the multi-phase coexistence in the past growth process. XPS data explains that the surface state of NbAs crystals will be affected by oxygen and lead to some changes, as specific results need to be further studied and discussed. In addition, we prepared a prototype of the NbAs photodetector in the visible light range and discussed the relationship between R and D* with the energy of incident photons. The result is equivalent to the report of the TaAs photodetector in the visible light range[30]. Our improved growth method provides reference and helps grow difficult-to-synthesize materials such as Weyl semimetal. At the same time, the synthesis of high-quality crystals guarantees the subsequent electrical properties research and photoelectric performance detection of this type of Weyl semimetal.

Author Contributions: Methodology, Y.Sun; validation, B.Zhao, Y.Sun. and Z.Huo; investigation, B.Zhao; data curation, Y.Sun; writing—original draft preparation, H.Qiu; writing—review and editing, H.Liu; project administration, Z. Hu. All authors have read and agreed to the published version of the manuscript.

Funding: This research was funded by the NSFC (51972229, 51802218, 51872198, 52172151), the Natural Science Foundation of Tianjin(19JCYBJC17800), National Defense Science and Technology 173 Program(2021-JCJQ-JJ-0639).

Acknowledgments: The authors thank Pro. W. C. Ma and Pro. L. J. Li for technical support.

Conflicts of Interest: The authors declare that they have no conflicts of interest.

References

1. Xu, S.-Y.; Alidoust, N.; Belopolski, I.; Yuan, Z.; Bian, G.; Chang, T.-R.; Zheng, H.; Strocov, V. N.; Sanchez, D. S.; Chang, G.; Zhang, C.; Mou, D.; Wu, Y.; Huang, L.; Lee, C.-C.; Huang, S.-M.; Wang, B.; Bansil, A.; Jeng, H.-T.; Neupert, T.; Kaminski, A.; Lin, H.; Jia, S.; Zahid Hasan, M. Discovery of a Weyl fermion state with Fermi arcs in niobium arsenide. *Nature Physics* **2015,** *11*, 748-754.
2. Huang, S. M.; Xu, S. Y.; Belopolski, I.; Lee, C. C.; Chang, G.; Chang, T. R.; Wang, B.; Alidoust, N.; Bian, G.; Neupane, M.; Sanchez, D.; Zheng, H.; Jeng, H. T.; Bansil, A.; Neupert, T.; Lin, H.; Hasan, M. Z. New type of Weyl semimetal with quadratic double Weyl fermions. *Proc Natl Acad Sci U S A* **2016**, *113 (5)*, 1180-5.
3. Yuan, X.; Zhang, C.; Zhang, Y.; Yan, Z.; Lyu, T.; Zhang, M.; Li, Z.; Song, C.; Zhao, M.; Leng, P.; Ozerov, M.; Chen, X.; Wang, N.; Shi, Y.; Yan, H.; Xiu, F. The discovery of dynamic chiral anomaly in a Weyl semimetal NbAs. *Nat Commun* **2020**, *11 (1)*, 1259.
4. Xu, Q.; Zhang, Y.; Koepernik, K.; Shi, W.; van den Brink, J.; Felser, C.; Sun, Y. Comprehensive scan for nonmagnetic Weyl semimetals with nonlinear optical response. *npj Computational Materials* **2020**, *6 (1)*.
5. Ji, Z.; Liu, G.; Addison, Z.; Liu, W.; Yu, P.; Gao, H.; Liu, Z.; Rappe, A. M.; Kane, C. L.; Mele, E. J.; Agarwal, R. Spatially dispersive circular photogalvanic effect in a Weyl semimetal. *Nat Mater* **2019**, *18 (9)*, 955-962.
6. Shekhar, C.; Nayak, A. K.; Sun, Y.; Schmidt, M.; Nicklas, M.; Leermakers, I.; Zeitler, U.; Skourski, Y.; Wosnitza, J.; Liu, Z.; Chen, Y.; Schnelle, W.; Borrmann, H.; Grin, Y.; Felser, C.; Yan, B. Extremely large magnetoresistance and ultrahigh mobility in the topological Weyl semimetal candidate NbP. *Nature Physics* **2015**, *11 (8)*, 645-649.
7. Yuan, X.; Yan, Z.; Song, C.; Zhang, M.; Li, Z.; Zhang, C.; Liu, Y.; Wang, W.; Zhao, M.; Lin, Z.; Xie, T.; Ludwig, J.; Jiang, Y.; Zhang, X.; Shang, C.; Ye, Z.; Wang, J.; Chen, F.; Xia, Z.; Smirnov, D.; Chen, X.; Wang, Z.; Yan, H.; Xiu, F. Chiral Landau levels in Weyl semimetal NbAs with multiple topological carriers. *Nat Commun* **2018**, *9 (1)*, 1854.
8. Osterhoudt, G. B.; Diebel, L. K.; Gray, M. J.; Yang, X.; Stanco, J.; Huang, X.; Shen, B.; Ni, N.; Moll, P. J. W.; Ran, Y.; Burch, K. S. Colossal mid-infrared bulk photovoltaic effect in a type-I Weyl semimetal. *Nat Mater* **2019**, *18 (5)*, 471-475.
9. Guo, C.; Tian, H. F.; Yang, H. X.; Sun, K.; Wei, L. L.; Chen, G. F.; Li, J. Q. Hexagonal Phase Intergrown with the Tetragonal Weyl Semimetal TaAs. *Crystal Growth & Design* **2017**, *17 (4)*, 1747-1751.
10. Boller, H.; Parthe, E. The Transposition Structure of NbAs and of Similar Monophosphides. *Acta Cryst* **1963**. *16*, 1095.
11. Li, Z.; Chen, H.; Jin, S.; Gan, D.; Wang, W.; Guo, L. Chen, X. Weyl Semimetal TaAs: Crystal Growth, Morphology, and Thermodynamics. *Crystal Growth & Design* **2016**, *16 (3)*, 1172-1175.
12. Sapkota, D.; Mukherjee, R.; Mandrus, D. Single Crystal Growth, Resistivity, and Electronic Structure of the Weyl Semimetals NbP and TaP. *Crystals* **2016**, *6 (12)*.
13. Lin; Guo; Dai; Lin; Hsu. PbI_2 Single Crystal Growth and Its Optical Property Study. *Crystals* **2019**, *9 (11)*.
14. Zhu, P.; Li, Y.; Yang, X.; Yang, Y.; Zhang, X.; Lin, X.; Yang, F.; Li, X.; Wang, Z. Synthesis of Superconducting InxSn1−xTe (0.04 < x < 0.1) Large Single Crystal by Liquid Transport Method. *Crystals* **2021**, *11 (5)*.
15. Panella, J. R.; Trump, B. A.; Marcus, G. G.; McQueen, T. M. Seeded Chemical Vapor Transport Growth of Cu2OSeO3. *Crystal Growth & Design* **2017**, *17 (9)*, 4944-4948.
16. Selter, S.; Shemerliuk, Y.; Büchner, B.; Aswartham, S. Crystal Growth of the Quasi-2D Quarternary Compound AgCrP2S6 by Chemical Vapor Transport. *Crystals* **2021**, *11 (5)*.
17. Sun, Z.; Liufu, S.; Chen, X.; Chen, L. Enhanced thermoelectric properties of $Bi_{0.5}Sb_{1.5}Te_3$ films by chemical vapor transport process. *ACS Appl Mater Interfaces* **2011**, *3 (5)*, 1390-3.
18. Saini, G. S.; Calvert, L. D.; Taylor, J.B. Prepation and Characterization of Crystals of MX- and MX_2 -Type of Niobium and Tantalum. *Division of Applied Chemistry* **1963**, *19*.
19. Zhang, M. D.; Hou, X. Y.; Wang, Q.; Wang, Y. Y.; Zhao, L. X.; Wang, Z.; Gu, Y. D.; Zhang, F.; Xia, T. L.; Ren, Z. A.; Chen, G. F.; Hao, N.; Shan, L. Tip-induced superconductivity on the topological semimetals $TaAs_2$ and $NbAs_2$. Physical Review B **2020**, *102 (8)*.
20. Wang, Yi. Yan.; Yu, Qiao. He.; Guo, Peng. Jie.; Liu, Kai.; Xia, Tian. Long. Resistivity plateau and extremely large magnetoresistance in $NbAs_2$ and $TaAs_2$. *Phys. Rev. B* **2016**, *94*, *041103(R).*
21. Greco, S.; Dal Zilio, S.; Bek, A.; Lazzarino, M.; Naumenko, D., Frequency Modulated Raman Spectroscopy. *ACS Photonics* **2017**, *5 (2)*, 312-317.
22. Liu, H. W.; Richard, P.; Song, Z. D.; Zhao, L. X.; Chen, G. F.; Ding, H. Raman study of lattice dynamics in the Weyl semimetal TaAs. *PHYSICAL REVIEW B* **2015**, *92*, 064302.
23. Chiarello, G.; Hofmann, J.; Li, Z.; Fabio, V.; Guo, L.; Chen, X.; Das Sarma, S.; Politano, A. Tunable surface plasmons in Weyl semimetals TaAs and NbAs. *Physical Review B* **2019**, *99 (12)*, 121401(R).
24. Bedoya-Pinto, A.; Pandeya, A. K.; Liu, D.; Deniz, H.; Chang, K.; Tan, H.; Han, H.; Jena, J.; Kostanovskiy, I.; Parkin, S. S. P. Realization of Epitaxial NbP and TaP Weyl Semimetal Thin Films. *ACS Nano* **2020**, *14 (4)*, 4405-4413.
25. Chi, S.; Li, Z.; Xie, Y.; Zhao, Y.; Wang, Z.; Li, L.; Yu, H.; Wang, G.; Weng.; H.; Zhang, H.; Wang, J.; . A Wide-Range Photosensitive Weyl Semimetal Single Crystal-TaAs. *Adv. Mater.* **2018**, *30*, 1801372.
26. Ross, J. S.; Klement, P.; Jones, A. M.; Ghimire, N. J.; Yan, J.; Mandrus, D. G.; Taniguchi, T.; Watanabe, K.; Kitamura, K.; Yao, W.; Cobden, D. H.; Xu, X. Electrically tunable excitonic light-emitting diodes based on monolayer WSe_2 p–n junctions. *Nat. Nanotechnol.* **2014**, *9*(4), 268-272. DOI: 10.1038/NNANO.2014.26.
27. Pezeshki, A.; Shokouh, S. H.; Nazari, T.; Oh, K.; Im, S. Electric and Photovoltaic Behavior of a Few-Layer α-$MoTe_2$/MoS_2 Dichalcogenide Heterojunction. *Adv. Mater.* **2016**, *28(16)*, 3216-3222. DOI: 10.1002/adma.201504090.

28. Zhang, S.; Guo, S.; Huang, Y.; Zhu, Z.; Cai, B.; Xie, M.; Zhou, W.; Zeng, H. Two-dimensional SiP: an unexplored direct band-gap semiconductor. *2D Materials* **2016**, *4*(1), 015030. doi:10.1088/2053-1583/4/1/015030.
29. Jing, Y.; Ma, Y.; Li, Y.; Heine, T. GeP_3: A Small Indirect Band Gap 2D Crystal with High Carrier Mobility and Strong Interlayer Quantum Confinement. *Nano Lett.* **2017**, *17*(3), 1833-1838. DOI: 10.1021/acs.nanolett.6b05143.
30. Chi, S.; Li, Z.; Xie, Y.; Zhao, Y.; Wang, Z.; Li, L.; Yu, H.; Wang, G.; Weng, H.; Zhang, H.; Wang, J. A Wide-Range Photosensitive Weyl Semimetal Single Crystal-TaAs. *Advanced Materials* **2018**, *30 (43)*.